Unravelling the Effect of Activators used in The Synthesis of Biomass-Derived Carbon Electrocatalysts on the Electrocatalytic Performance for CO_2 Reduction

Fu, Shilong; Li, Ming; Asperti, Simone; de Jong, Wiebren; Kortlever, Ruud

DOI
10.1002/cssc.202202188

Publication date
2023

Document Version
Final published version

Published in
ChemSusChem

Citation (APA)
Fu, S., Li, M., Asperti, S., de Jong, W., & Kortlever, R. (2023). Unravelling the Effect of Activators used in The Synthesis of Biomass-Derived Carbon Electrocatalysts on the Electrocatalytic Performance for CO_2 Reduction. *ChemSusChem*, *16*(9), Article e202202188. https://doi.org/10.1002/cssc.202202188

Chemistry Europe
European Chemical Societies Publishing

WILEY VCH

Excellence in Chemistry Research

Announcing our new flagship journal

- Gold Open Access
- Publishing charges waived
- Preprints welcome
- Edited by active scientists

Meet the Editors of *ChemistryEurope*

Luisa De Cola
Università degli Studi di Milano Statale, Italy

Ive Hermans
University of Wisconsin-Madison, USA

Ken Tanaka
Tokyo Institute of Technology, Japan

ChemSusChem

Research Article
doi.org/10.1002/cssc.202202188

Chemistry Europe
European Chemical Societies Publishing

www.chemsuschem.org

Unravelling the Effect of Activators used in The Synthesis of Biomass-Derived Carbon Electrocatalysts on the Electrocatalytic Performance for CO_2 Reduction

Shilong Fu,[a] Ming Li,[a, b] Simone Asperti,[a] Wiebren de Jong,[a] and Ruud Kortlever*[a]

N-doped carbon materials can be efficient and cost-effective catalysts for the electrochemical CO_2 reduction reaction (CO_2RR). Activators are often used in the synthesis process to increase the specific surface area and porosity of these carbon materials. However, owing to the diversity of activators and the differences in physicochemical properties that these activators induce, the influence of activators used for the synthesis of N-doped carbon catalysts on their electrochemical performance is unclear. In this study, a series of bagasse-derived N-doped carbon catalysts is prepared with the assistance of different activators to understand the correlation between activators, physicochemical properties, and electrocatalytic performance for the CO_2RR. The properties of N-doped carbon catalysts, such as N-doping content, microstructure, and degree of graphitization, are found to be highly dependent on the type of activator applied in the synthesis procedure. Moreover, the overall CO_2RR performance of the synthesized electrocatalysts is not determined only by the N-doping level and the configuration of the N-dopant, but rather by the overall surface chemistry, where the porosity and the degree of graphitization are jointly responsible for significant differences in CO_2RR performance.

Introduction

The electrochemical CO_2 reduction reaction (CO_2RR) is a promising approach to close the carbon cycle and convert CO_2 into value-added chemicals and fuels.[1–3] This process can be driven by renewable electricity sources such as solar and wind and conducted at ambient conditions, making it an attractive option for energy storage and the electrification of the chemical industry.[4] However, the thermodynamic stability of CO_2 and the competition with the hydrogen evolution reaction (HER), taking place in the same potential window as the CO_2RR in aqueous electrolytes, hinders the development of the CO_2RR.[5] Challenges that need to be overcome include slow kinetics, high overpotentials for the formation of products and low product selectivities.[6–8] Thus, developing more efficient and selective electrocatalysts for the CO_2RR is highly desired. Various metal-based CO_2RR electrocatalysts containing, for instance, Ag,[9] Au,[10] Pd,[11] Pt,[12] Zn,[13] Sn,[14] and Cu,[15,16] have been extensively studied in the past few decades. Although some advanced metal-based catalysts exhibit a very high product selectivity and impressive overall catalytic performance, their relatively high cost, limited availability, and poor stability hinder large-scale applications.[17,18] Therefore, the development of sustainable low-cost catalysts is crucial.

Metal-free carbon-based electrocatalysts, especially nitrogen-doped carbon materials, have recently attracted increasing attention owing to their interesting properties. These materials have a relatively low price, high conductivity, high stability, strong tolerance to impurities and a good structure tenability.[18–21] N-doped carbon materials have been used as catalysts for the CO_2RR to produce CO,[22–24] CH_4,[25] HCOOH,[26,27] and even multi-carbon products such as ethanol.[28] However, most of these carbon materials are derived from fossil feedstocks and their production processes are energy-intensive with generally low yields. Moreover, the harsh synthesis conditions to prepare these materials hamper the scale-up needed for industrial utilization.[29]

Biochar, carbon derived from biomass carbonization, can be a sustainable source to prepare cost-effective carbonaceous catalysts.[30,31] Additionally, the unique natural microstructures and specific chemical compositions of biomass precursors endow the derived carbon materials with ingenious porous structures, high surface areas, abundant defect sites, and heteroatom doping that can improve the electrocatalytic performance.[32–34] Additional heteroatom doping and the use of activators, to respectively provide more active sites and enlarge the specific surface area and porosity are often part of the preparation procedure to produce biomass-derived carbon electrocatalysts.[35] Biomass-derived N-doped carbon materials have already been demonstrated as effective electrocatalysts for the oxygen reduction reaction (ORR),[36,37] whereas a limited amount of studies report on their performance for the CO_2RR. Li

[a] S. Fu, M. Li, S. Asperti, Prof. Dr. W. de Jong, Dr. R. Kortlever
Process & Energy Department, Faculty of Mechanical, Maritime and Materials Engineering
Delft University of Technology
Leeghwaterstraat 39, 2628 CB Delft (The Netherlands)
E-mail: R.Kortlever@tudelft.nl
[b] M. Li
Chemical Engineering Department, Faculty of Applied Sciences
Delft University of Technology
Van der Maasweg 9, 2628 HZ Delft (The Netherlands)

Supporting information for this article is available on the WWW under https://doi.org/10.1002/cssc.202202188

et al.[38] prepared a porous N-doped carbon electrocatalyst from wheat flour carbonization, using KOH as activator, showing CO_2 reduction to CO with a maximum faradaic efficiency (FE) of 83.7% at −0.82 V vs. RHE. Hao et al.[39] synthesized a cedar wood biomass-derived three-dimensional (3D) N-doped graphitized carbon electrocatalyst, using an $FeCl_3$ activator, that achieved a 91% FE toward CO at −0.56 V vs. RHE.

The activation process has been shown to significantly affect the textural properties of carbon catalysts, such as the specific surface area, porosity, N-doping content and the degree of graphitization. Most of the studies investigating activated N-doped carbon electrocatalysts attribute the electrocatalytic performances to the larger specific area and higher N-doping content.[40] However, the effect of other structural properties, such as the porosity and the degree of graphitization, have been largely overlooked. A comprehensive analysis that couples the physicochemical properties of N-doped carbon electrocatalysts after the activation process with the resultant electrochemical performances is therefore highly desired. However, currently there is no systematic study linking the effects of activators used in the preparation of biomass-derived carbon electrocatalysts for the CO_2RR to the electrocatalytic performance.

Here, we report a series of systematic experiments to unravel the effect different activators have on the CO_2RR performance of biomass-derived N-doped carbon materials. In this study, we are not aiming to develop a robust catalyst with an impressive performance but aim to understand how the applied activator influences the properties of the N-doped carbon and subsequently influences the electrochemical performance. Sugarcane bagasse was selected as the carbon precursor, as it is an abundantly available and easily collected biomass residue from sugar production. Various N-doped porous carbon catalysts were synthesized with the assistance of urea as nitrogen source and different activators, KOH, $KHCO_3$, K_2CO_3, NaOH, $NaHCO_3$, and $Mg_5(OH)_2(CO_3)_4$, using a one-step pyrolysis method. We show that the activators play a critical role during the carbonization process, and the choice of activator significantly affects the resulting electrocatalytic performance of the material for the CO_2RR. The best biomass-derived catalyst exhibited a maximum FE_{CO} of 80% and a partial current density j_{CO} of $-2.31\ mA\,cm^{-2}$ at −0.93 V vs. RHE, whereas the worst catalyst has a very limited activity for the CO_2RR, only displaying a FE_{CO} of 6.9% with a j_{CO} of less than $-0.01\ mA\,cm^{-2}$. Combining the results of the physicochemical characterization with the electrochemical performance, we find that the overall CO_2RR performance is not only dominated by the N-doping level, but is also dependent on the interplay of the microstructure and the degree of graphitization of the material.

Results and Discussion

Characterization of the biomass-derived materials

The porous carbon catalysts were prepared by a one-step pyrolysis method. The morphology of the sugarcane bagasse before carbonization, the prepared biochar (BC), N-doped biochar (NBC), and all activated N-doped biochar (ANBC) samples were visualized by SEM (Figure 1 and Figure S1 in the Supporting Information).

The sugarcane bagasse shows a long vascular fiber structure. The original BC sample derived from pure bagasse pyrolysis is composed of larger particles with a smooth surface. When urea was added as a nitrogen source, the surface became rougher in comparison to BC. This can be associated to the etching effect of NH_3, which is released by urea decomposition during the pyrolysis procedure. For ANBC3 ($Mg_5(OH)_2(CO_3)_4$), the morphology did not show a significant difference with BC, as only bulk particles with no visible pores on the surface are observed. The addition of other activators created higher

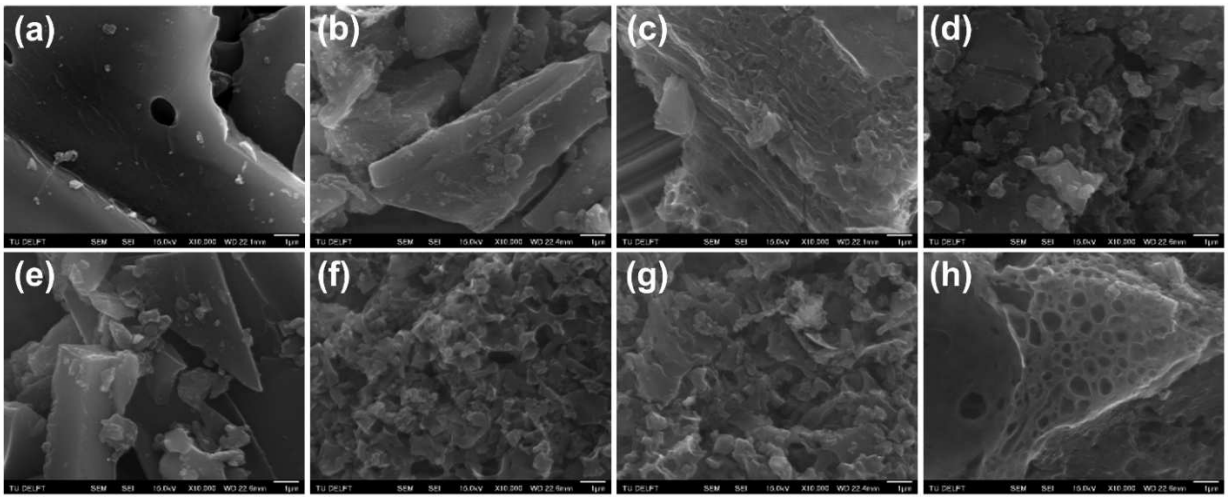

Figure 1. SEM images of different biomass-derived carbon catalysts: (a) BC; (b) NBC; (c) ANBC1($NaHCO_3$); (d) ANBC2 (K_2CO_3); (e) ANBC3 ($Mg_5(OH)_2(CO_3)_4$); (f) ANBC4 (NaOH); (g) ANBC5 (KOH); (h) ANBC6 ($KHCO_3$). Scale bar is 1 μm.

porosity in the carbon samples. ANBC1 ($NaHCO_3$), ANBC2 (K_2CO_3), and ANBC6 ($KHCO_3$) maintain a similar bulk shape as the NBC, while developing a highly porous structure due to the etching effect of the activators. For ANBC4 (NaOH) and ANBC5 (KOH), the bulk carbon was etched into smaller particles, with a large number of porous structures formed by stacking between the particles, exhibiting a hierarchically porous structure with an interconnected carbon matrix. Energy-dispersive X-ray spectroscopy (EDX; Figure S2) revealed only the presence of carbon, nitrogen, oxygen, and silicon. This indicates that residues of the activators have been successfully washed out. The observed silicon originates from the biomass cultivation process and cannot be removed by acid washing. Although carbon and nitrogen show consistent dispersion in the elemental mapping, the carbon (0.282 eV) and nitrogen (0.392 eV) peaks in the EDX spectra overlap due to the influence of inter-elemental interference.[41] Hence, the presence of nitrogen will be double-checked by XPS. To further visualize the microstructure of the samples, TEM measurements were carried out (Figure S3). Samples BC, NBC, and ANBC3 ($Mg_5(OH)_2(CO_3)_4$) exhibit a carbon structure with stacked carbon layers that mainly consists of micropores. Mesopores formed during the activation process can be easily observed for the other samples. Thereby, the activation process both increases the specific surface area of the catalysts and promotes the mass transfer of reactants and products into the carbon catalysts by the formation of mesopores. This can improve the accessibility of active sites, which can potentially contribute to improving the CO_2RR performance of the materials.

N_2 adsorption-desorption isothermal analyses were performed to quantify the specific surface areas and pore size distributions of the samples. As shown in Figure 2a, the increase of all isotherms at very low relative pressure indicates the presence of micropores in all samples. A higher adsorption value at very low relative pressures indicates a larger micropores-derived pore volume. For BC and NBC, the total adsorption quantity remains almost constant with the increase of relative pressure, showing a type I isotherm behavior according to the IUPAC classification, indicating that these catalysts only possess microporosity.[42] For ANBC3 ($Mg_5(OH)_2(CO_3)_4$), the isotherm shows a small amount of microporous adsorption. In addition, a negligible type IV hysteresis loop was observed (Figure S4a), indicating that mesoporous structures were successfully created in the carbon matrix despite the very small specific surface area (Table S1). The isotherms of other samples display a combination of a type I and type IV isotherms, with an obvious hysteresis loop of type H4 at $P/P_0 = 0.45–0.95$, suggesting the presence of

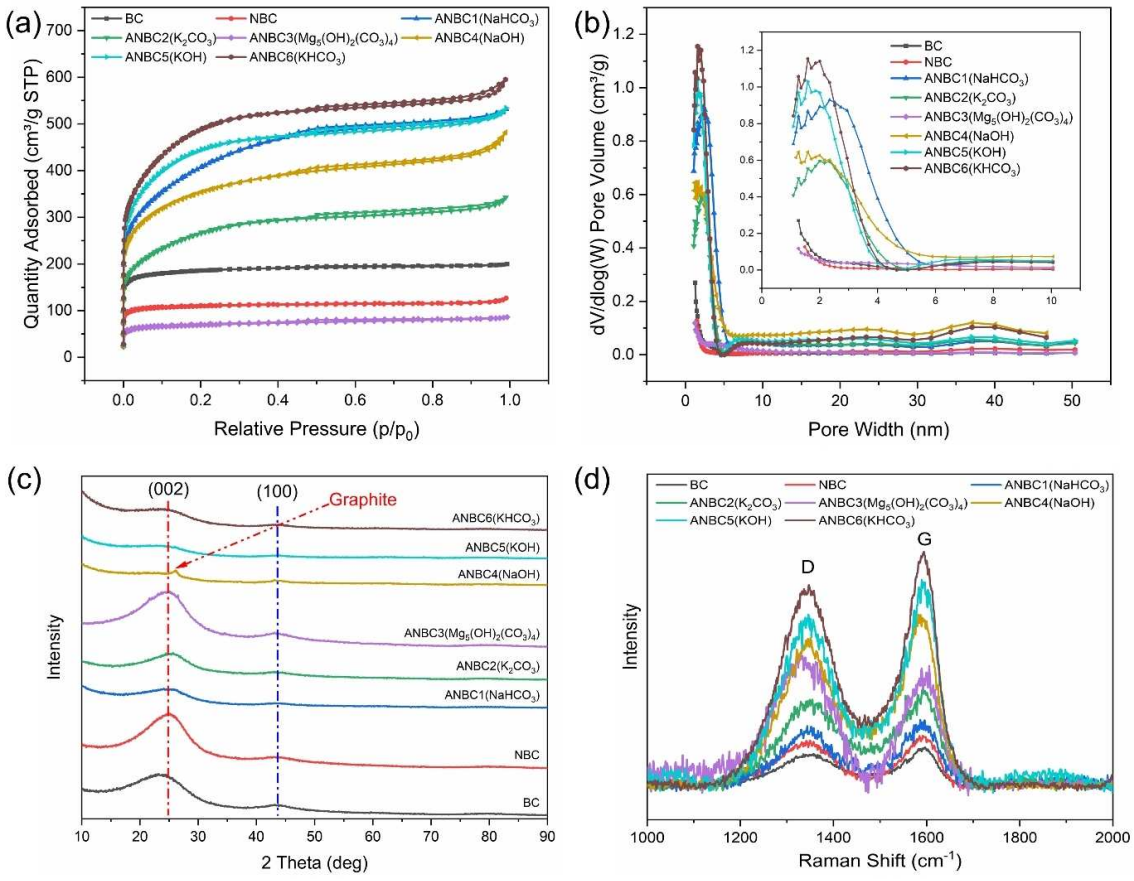

Figure 2. (a) N_2 adsorption-desorption isotherms; (b) pore size distributions; (c) XRD patterns; and (d) Raman spectra of different biomass-derived carbon catalysts.

mesopores.[43] The increasing trends at the higher relative pressure regime ($P/P_0 > 0.95$) indicate the existence of macropores in these samples.[44] As can be seen from the pore size distribution plots (Figure 2b), samples BC and NBC mainly have narrow micropores of pore sizes lower than 1 nm. ANBC3 ($Mg_5(OH)_2(CO_3)_4$) shows a pore size distribution with narrow micropores, with the additional formation of some mesopores (ca. 4 nm; Figure S4b). The other samples exhibit a broad pore size distribution including wider micropores (1–2 nm), narrow mesopores (2–6 nm), and a small amount of large mesopores (35–45 nm). Such a hierarchically porous structure with a strong adsorption behavior can potentially enhance the adsorption of CO_2 and facilitate the diffusion of both the reactants and products, thereby improving the electrocatalytic performance of the material.[45,46]

The specific surface areas and pore volumes measured are summarized in Table S1. Sample BC exhibits a specific surface area of 724.8 $m^2 g^{-1}$ with a total pore volume of 0.3 $cm^3 g^{-1}$. After introducing urea as a nitrogen source, the specific surface area and pore volume of NBC decreases to 431.6 $m^2 g^{-1}$ and 0.18 $cm^3 g^{-1}$, respectively. Moreover, the sample ANBC3 ($Mg_5(OH)_2(CO_3)_4$) displays an even worse porosity with a lower specific surface area and pore volume. This is due to the thermal decomposition of urea and $Mg_5(OH)_2(CO_3)_4$ in the carbonization process, which absorbs a large amount of heat. This inhibits the carbonization of bagasse, resulting in worse textural properties (Table S1). By contrast, the other activators created abundant pores, resulting in specific surface areas from 960.5 to 1786.9 $m^2 g^{-1}$, and pore volumes from 0.50 to 0.87 $cm^3 g^{-1}$. The enlarged surface area is conducive to exposing more active sites and thereby can improve the catalytic performance.[47] It is noteworthy that the mesopore ratios and average pore sizes of the different carbon samples are highly related to the properties of the activators (Table S1). ANBC3 ($Mg_5(OH)_2(CO_3)_4$) and ANBC4 (NaOH) have a higher ratio of mesopores than other samples, while ANBC1 ($NaHCO_3$) and ANBC4 (NaOH) exhibit a larger average pore size. Both of these properties are considered to be key factors affecting mass transfer processes during the CO_2RR. In general, the larger specific surface area can expose more active sites, while the porosity (pore size distribution and average pore size) affects the accessibility of the reactant to active sites. A good balance between specific surface area and porosity can therefore help to improve the performance of the carbon catalyst.

XRD was used to determine the crystallographic structure of the as-prepared carbon samples (Figure 2c). All samples exhibit an analogous diffraction feature with two broad peaks located at about $2\theta = 25°$ and 44°, which are assigned to the diffraction of the (002) plane and (100) plane of graphitic-like carbon, respectively.[48] The peak located at around $2\theta = 25°$ suggests a disordered amorphous carbon structure.[48] For the nonactivated biochar sample (BC), the peak shifted to a smaller angle, indicating a relatively low degree of crystallinity.[49] A tiny sharp peak appeared at the right side of the (002) peak for ANBC4 (NaOH) and was identified as a signal of graphite,[50] indicating that this sample is more graphitized than the other samples. The low intensity peak located at 44° was attributed to graphitic carbon with a limited degree of graphitization.[51] The local disorder and graphitization of the carbon samples was determined by Raman spectroscopy measurements. All carbon samples presented two peaks at around 1350 and 1580 cm^{-1}, corresponding to the D band and G band, respectively (Figure 2d).[52] The D band derives from crystal defects and the disordered structure of carbon, while the G band relates to the lattice vibration of sp^2-hybridized graphitic carbon.[53] Generally, the intensity ratio between the D and G band (I_D/I_G) is adopted as an index to evaluate the degree of graphitization of carbon materials. A high I_D/I_G value signifies a lower degree of graphitization.[54] Here, we observe that the value of I_D/I_G increases after activation, indicating that more defects and disordered carbon lattice structures were generated during the activation processes (Table S1). The more disordered structure is associated with a larger surface area and provides more defects that can act as active sites.[55] However, a higher degree of graphitization enhances the electrical conductivity of carbon materials, hence facilitating electron/charge transfer and potentially improving the catalytic performance.[56] Therefore, the optimal graphitization degree of carbon catalysts is a trade-off between a more activated surface and a material with higher conductivity.

To elucidate the chemical surface composition of all carbon samples, XPS measurements were performed. The full survey spectra of the samples are presented in Figure S5, and the elemental compositions are summarized in Table S2. Three strong signals were detected for all carbon samples, which were attributed to C1s, N1s, and O1s peaks. Trace amounts of silicon were detected on the as-prepared catalysts after the acid treatment. The observed silicon originates from the biomass cultivation process and cannot be removed by acid washing. It is noted that the BC had a 1.05% N content, stemming from the pyrolysis of the original proteins or N-functional groups on lignin. Compared with the biochar without modification, the NBC exhibited a 10.81% N content due to the addition of urea in the pyrolysis process. With the use of activators, the N content decreased to 3.85–8.7%, indicating that the activators regulate the chemical composition of the carbon samples. Some powerful activators such as KOH and NaOH, remove nitrogen and oxygen functional groups on the carbon surface during the activation process, resulting in a lower N-doping content. However, for sample ANBC3, the use of $Mg_5(OH)_2(CO_3)_4$ hindered carbonization and lowered the C content to 77.3% while creating disordered structures, which is in good agreement with the Raman spectroscopy results. In conclusion, nitrogen was successfully doped into the matrix of biomass-derived carbon samples via the one-step pyrolysis method, whereas the doping content strongly depended on the type of activator used.

To further investigate the type of N-containing species present in the carbon catalysts, high-resolution N1s spectra (Figure 3) were deconvoluted into four individual peaks at around 398.2, 399.9, 401.6, and 404.4 eV, referring to pyridinic N, pyrrolic N, graphitic N, and oxidized N, respectively.[51,57,58] The blank BC only contained pyrrolic N species while other N species were detected when urea was used as nitrogen source.

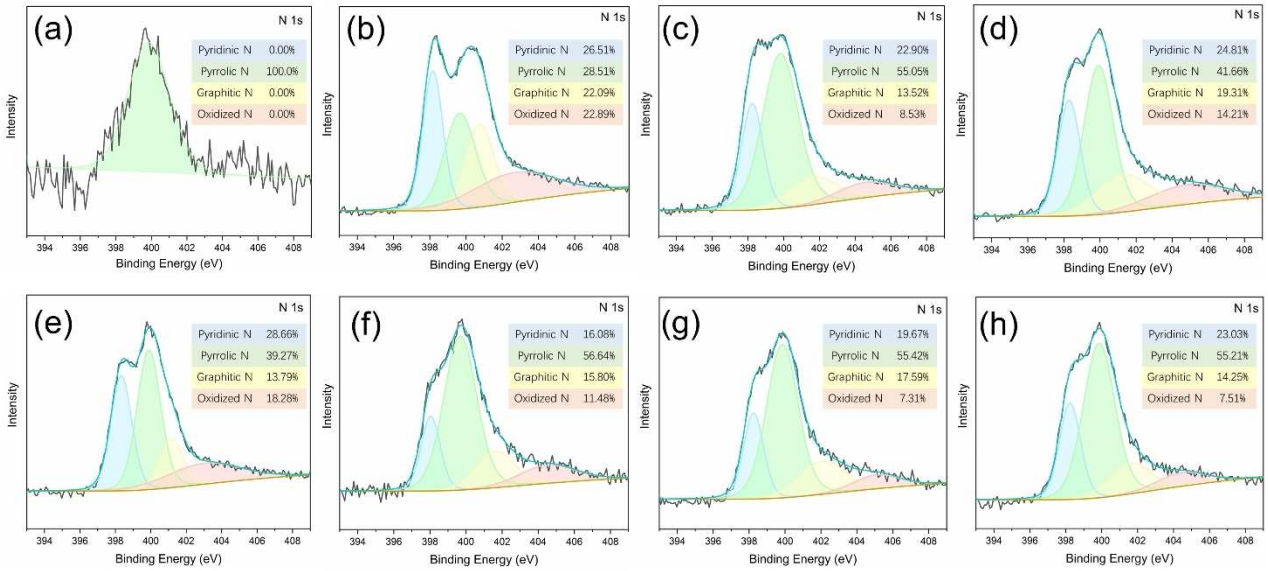

Figure 3. High-resolution N1s spectra of different biomass-derived carbon catalysts: (a) BC; (b) NBC; (c) ANBC1 ($NaHCO_3$); (d) ANBC2 (K_2CO_3); (e) ANBC3 ($Mg_5(OH)_2(CO_3)_4$); (f) ANBC4 (NaOH); (g) ANBC5 (KOH); (h) ANBC6 ($KHCO_3$). Intensity is given in arbitrary units.

As shown in Figure 3 and Table S2, the used activators play a crucial role in controlling the distribution of N-bonding configurations on the carbon surface. In general, pyrrolic N is the main nitrogen-containing species observed, followed by pyridinic N, graphitic N, and oxidized N. The existence of oxidized N is attributed to the strong reaction between urea and the oxygen functional groups of the biomass-derived carbon surface.[59] The N-doping changes the charge and spin distribution in the N dopant and adjacent C atoms, which enhances the interaction with reactants for dissociative adsorption and facilitates the electron donor-acceptor charge transfer to improve the electrocatalytic performance.[30,60,61] Interestingly, both pyridinic N and graphitic N were demonstrated as the active sites for the CO_2RR by experimental results and theoretical calculations.[62,63] However, owing to the complexity of the reaction mechanisms and N dopant properties, the role of these N containing active sites during the CO_2RR is still under debate. The fitted C1s and O1s spectrum are shown in Figures S6 and S7. The high-resolution C1s spectrum can be split into three peaks at around 284.8, 285.5, and 288.5 eV, which can be assigned to C–C, C–N, and C–O, respectively.[36] The high-resolution O1s spectrum can be fitted by three peaks at around 530.6, 532.5, and 535.0 eV, representing O–N, O=C, and O–C, respectively.[64]

Understanding the effect of activators

$Mg_5(OH)_2(CO_3)_4$ has previously been used as an activator to produce porous carbon materials.[36,65] During the carbonization process, $Mg_5(OH)_2(CO_3)_4$ gradually decomposes into MgO, CO_2, and H_2O, where the nanocrystals of MgO are embedded in the carbon structure as a template, endowing the carbon material with a rich mesoporous structure after acid washing, while CO_2 and H_2O are involved in the activation of the carbon material as physical activators and give it a rich microporous structure.[65] As shown in Table S1, ANBC3 ($Mg_5(OH)_2(CO_3)_4$) exhibited a higher ratio of mesopores than other catalysts, which should be beneficial for mass transfer during the CO_2RR. However, the one-step pyrolysis method resulted in only limited interaction between the bagasse and the activator, leading to a similar morphology as BC and keeping a relatively high N-doping content. In addition, the excess amount of $Mg_5(OH)_2(CO_3)_4$ absorbed a large amount of heat during decomposition, which resulted in poor carbonization of the sample, showing a higher I_D/I_G value and a smaller specific surface area.

NaOH and $NaHCO_3$ are two commonly used chemical activators and are both capable of producing carbon samples with a well-developed pore structure.[66] NaOH works as an oxidant, oxidizing the carbon framework and thereby improving the porosity.[67] $NaHCO_3$ is considered a chemical foaming agent,[68] as it decomposes during carbonization, releasing large amounts of CO_2 and H_2O, which leads to the formation of a hierarchical porosity. Interestingly, both NaOH and $NaHCO_3$ decompose to form Na_2CO_3. The Na_2CO_3 is embedded in the carbon matrix and acts as a template to provide a large number of mesopores for the carbon material.[69] Indeed, sample ANBC4 (NaOH) and ANBC1 ($NaHCO_3$) showed a larger ratio of mesoporous structure and larger average pore diameter than other catalysts (Table S1). In particular, owing to the strong oxidizing properties of NaOH, the carbon framework is strongly etched resulting in ANBC4 (NaOH) showing smaller particles and a relatively low N-doping content. As for ANBC1 ($NaHCO_3$), the porosity is well developed while keeping a higher N-doping content. In short, NaOH and $NaHCO_3$ endow the catalysts with a large specific area, rich mesoporosity and effective N-doping.

Potassium salts, such as KOH, $KHCO_3$, and K_2CO_3 are also widely used as activators to endow high porosity to lignocellu-

lose-derived carbon materials. However, their activation characteristics lead to variations in structures and properties of the biochar. KOH reacts with carbon at high temperatures, generating various potassium species (K_2CO_3, K_2O, K) and releasing a large amount of gas (CO_2, H_2O). This leads to etching of the carbon matrix by redox reactions, and samples with a large specific surface area and high microporosity are obtained (Table S1).[70] In addition, KOH has a low fusion point (ca. 380 °C) and the molten salt results in the disintegration of the carbon material, which roughens the surface and forms small particles (Figure 1g).[71] The activation mechanism of $KHCO_3$ is similar to that of $NaHCO_3$.[72] $KHCO_3$ decomposes at around 200 °C to K_2CO_3 and releases gases, which develop macropores in the carbon matrix. The released CO_2 and H_2O are further involved in the activation process, producing additional micropores or further enlarging the existing pore structure.[53] By contrast, K_2CO_3 is more stable than KOH and $KHCO_3$ (the fusion point of K_2CO_3 is approximately 890 °C), and its activation performance is strongly dependent on the pyrolysis temperature. Some studies point out that K_2CO_3 has a time-dependent reduction and decomposition starting from 700 °C to produce K_2O, K, and CO_2, which further improves the porosity.[71] The longer the residence time, the larger the specific surface area and the higher the porosity.[73] When the temperature reaches 900 °C, K_2CO_3 melts and this results in the shrinkage and collapse of porous structures.[53] In this study, ANBC5 (KOH) and ANBC6 ($KHCO_3$) exhibited a similar degree of graphitization, whereas these activators developed a larger specific surface and a higher pore volume than other samples (Table S1). However, the dominance of micropores can induce a higher mass transfer resistance during the CO_2RR, which potentially hinders the catalytic performance. Although ANBC2 (K_2CO_3) showed a higher N-doping content, it did not generate a well-developed porous structure due to the short pyrolysis residence time (1 h), with its specific surface area only reaching about 960 $m^2 g^{-1}$ and the porosity being mostly composed of micropores.

Electrochemical performance

To evaluate the electrochemical performance of the prepared catalysts, linear sweep voltammetry (LSV) was performed in an Ar-saturated and CO_2-saturated aqueous 0.1 M $KHCO_3$ electrolyte. As shown in Figure S8, the current densities of BC, NBC, and ANBC3 ($Mg_5(OH)_2(CO_3)_4$) were lower in a CO_2-saturated electrolyte than in an Ar-saturated electrolyte over the entire potential range, indicating that these catalysts have little activity for the CO_2RR. By contrast, ANBC1 ($NaHCO_3$), ANBC2 (K_2CO_3), ANBC4 (NaOH), ANBC5 (KOH), and ANBC6 ($KHCO_3$) exhibited higher current densities in the CO_2-saturated electrolyte at more negative potentials, beyond −0.7 V vs. RHE, indicating that they are active electrocatalysts for the CO_2 reduction reaction. A comparison of the LSVs with different samples in a CO_2-saturated electrolyte is shown in Figure 4a. Due to the different physicochemical properties of the catalysts, significant differences in the LSV results can be observed. ANBC3 ($Mg_5(OH)_2(CO_3)_4$) showed an almost negligible current density due to its low specific surface area and low degree of graphitization. In contrast, ANBC4 (NaOH) exhibited better CO_2 electrocatalytic activity than other samples, displaying a lower onset potential and higher current density. This can be attributed to the larger surface area and hierarchically porous structure of the ANBC4 (NaOH) sample. However, as the trends in current density observed in the voltammograms is not decisive evidence for CO_2 reduction activity, direct evidence for the formation of CO_2 reduction products is needed.

To thoroughly evaluate the electrocatalytic performance of the various carbon materials for the CO_2RR, chronoamperometry measurements were conducted at various potentials from −0.50 to −1.15 V vs. RHE. For all the samples, CO and H_2 were the main gaseous products observed, while trace amounts of CH_4 with a FE for CH_4 lower than 1% could be detected when the applied potential was more negative than −0.8 V vs. RHE. Besides these gaseous products, no liquid products were detected by HPLC. The FEs of CO and H_2 obtained at the tested potentials for all the samples are plotted in Figure 4b and Figure S9a, respectively. The BC, NBC, and ANBC3 ($Mg_5(OH)_2(CO_3)_4$) electrocatalysts exhibited a poor selectivity toward CO and produce H_2 as the dominant product. These performances are consistent with the LSV results, indicating that these materials are poor CO_2 reduction catalysts. For ANBC1 ($NaHCO_3$), ANBC2 (K_2CO_3), ANBC4 (NaOH), ANBC5 (KOH), and ANBC6 ($KHCO_3$), the product selectivity was strongly dependent on the applied potential (Figure 4b). With a decrease in applied potential, the trend of CO selectivity displays a volcano-like curve. Among these materials, ANBC4 (NaOH) exhibited the highest FE_{CO} of 80% at −0.93 V vs. RHE, while ANBC5 (KOH) reached 74.4% at the same potential, whereas the maximum FE_{CO} for ANBC1 ($NaHCO_3$), ANBC2 (K_2CO_3), and ANBC6 ($KHCO_3$) was 42.4%, 45.8%, and 46.0% at −0.91 V vs. RHE, −1.00 V vs. RHE and −0.80 V vs. RHE, respectively. With a further decrease of applied potential, the CO selectivity reduced gradually, and H_2 production regained dominance at the more negative potentials. Meanwhile, the FE_{H2} presented an opposite trend (Figure S9a), with ANBC4 (NaOH) and ANBC5 (KOH) exhibiting the lowest selectivity toward H_2. It should be noted that the total FE was below 100% at the more positive potentials due to low current densities resulting in product concentrations below or near the detection limit of the gas chromatograph, such that the FE cannot accurately be calculated.[74]

The total current density and partial current densities j_{CO} and j_{H_2} are plotted in Figure 4c,d and Figure S9b, respectively. The total current density of all prepared catalysts increased with more negative potentials. Notably, carbon catalysts activated with the sodium salts (NaOH, $NaHCO_3$) exhibited greater current densities than those activated by potassium salts (KOH, $KHCO_3$, K_2CO_3). As for the j_{CO}, except for BC, NBC, and ANBC3 ($Mg_5(OH)_2(CO_3)_4$), which are not catalytically active, the other catalysts show a similar trend, where the j_{CO} increases first and then decreases when the potential becomes more negative. Especially ANBC4 (NaOH) presented a significantly higher total current density and j_{CO} in comparison to the other samples. In the potential range between −0.8 V to −1.0 V vs. RHE, j_{CO} is

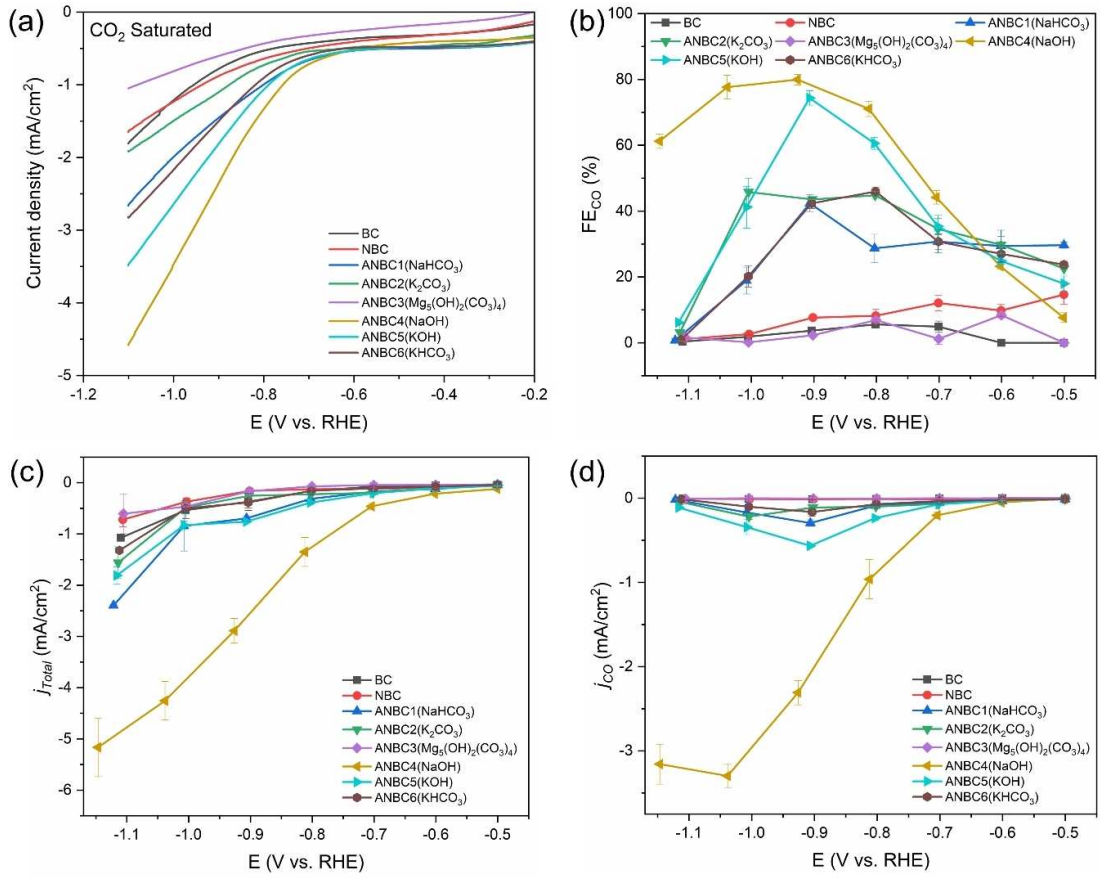

Figure 4. (a) LSV curves recorded at a scan rate of 5 mV s^{-1} of all catalysts in a CO_2-saturated 0.1 M $KHCO_3$ electrolyte; (b) FE of CO production at applied potentials from −0.50 to −1.15 V vs. RHE; (c) Total current density of all catalysts at different applied potentials; (d) Partial current density of CO of all catalysts at different applied potentials.

higher than j_{H_2}, indicating that the CO_2 reduction is the dominant reaction.

The electrochemically active surface area (ECSA) of each catalyst was determined by the double layer capacitance (C_{dl}), which was determined with cyclic voltammetry measurements in the nonfaradaic region. As shown in Figure S10, the C_{dl} values of these ANBCs are positively correlated with their specific area, corresponding to earlier results by Taer et al.[75] Although ANBC6 ($KHCO_3$) and ANBC1 ($NaHCO_3$) showed a higher ECSA than other samples, their catalytic performances were not as good as ANBC4 (NaOH) and ANBC5 (KOH). This means that not all electrochemically active sites show catalytic activity for the CO_2RR. This is in line with results of Voiry et al.,[76] who report that nonactive carbon can lead to an overestimation of the ECSA and an underestimation of the catalytic performance.

In addition, the charge transfer resistance also has a crucial effect on the current density, as smaller charge transfer resistances lead to a larger current density. The Nyquist plots of each sample are depicted in Figure S11. ANBC4 (NaOH) and ANBC5 (KOH) showed lower interfacial charge transfer resistance than other samples, demonstrating more rapid electron transfer than the other samples in CO_2RR process.[60] In general, the high FE_{CO} and small charge transfer resistance of ANBC4 (NaOH) gives it a superior electrocatalytic performance over other samples.

To investigate the kinetics of the CO_2RR on various catalysts, a Tafel slope analysis of ANBC1 ($NaHCO_3$), ANBC2 (K_2CO_3), ANBC4 (NaOH), ANBC5 (KOH), ANBC6 ($KHCO_3$) was conducted (Figure S12). ANBC4 (NaOH) exhibited a lower Tafel slope (155 mV dec^{-1}) than that of the other 4 samples, indicating that ANBC4 (NaOH) has faster kinetics for CO_2 reduction to CO. The other samples showed a Tafel slope between 226 and 382 mV dec^{-1}. Since a Tafel slope close to 118 mV dec^{-1} indicates that the rate-determining step of the CO_2RR is a single-electron transfer process, where CO_2 absorbs the first electron to generate the $*CO_2^-$ intermediates,[60] these higher Tafel slope values indicate that other processes determine the kinetics of the CO_2RR on these materials. Consequently, we hypothesize that the rate-determining step for ANBC1 ($NaHCO_3$), ANBC2 (K_2CO_3), ANBC5 (KOH), and ANBC6 ($KHCO_3$) is the diffusion of CO_2 from the electrolyte to the active sites.[40]

Control experiments to verify whether the observed CO was produced from CO_2 were carried out using ANBC4 (NaOH) and ANBC5 (KOH) at an applied potential of −0.9 V vs. RHE in Ar-saturated 0.1 M $KHCO_3$ electrolyte. Only H_2 was detected with Ar-saturated electrolytes (Figure S13), indicating that the ob-

served CO only originates from electrochemical CO_2 reduction and not from the disintegration of functional groups on the carbon surface.

Understanding the structure-activity relationship

To get an understanding of how the structure and composition of the carbon catalysts affects the electrocatalytic performance, we will here combine the results of the physicochemical characterization with the results of electrochemical testing. Generally, the higher N-doping content and larger specific surface area are considered as the most important parameters to enhance the CO_2RR performance of N-doped carbon materials. However, several studies have shown impressive performances with lower specific surface areas and lower N-doping contents.[77–79] Therefore, we think that overemphasizing the impact of one or two factors on the overall catalytic performance can lead to lopsided conclusions. To avoid this, a comprehensive analysis of the effect of the physicochemical properties of the carbon catalyst on the catalytic performance is essential.

Introducing N as a heteroatom into a carbon matrix can modulate the charge distribution on the carbon surface and provide active sites for the CO_2RR. In addition, previous studies have demonstrated that the adsorption behavior of CO_2 can be improved by introducing N into the carbon matrix.[22,80] Many studies have demonstrated through experimental analyses and theoretical calculations that the product selectivity and the activity of N-doped carbon materials for the CO_2RR strongly depends on the N doping content.[24,81] Both pyridinic N and graphitic N have been reported as the active sites for the CO_2RR.[63] Some studies have set out to improve the catalytic performance of N-doped carbon catalysts by enhancing the N-doping content or by controlling the preparation conditions to increase the ratio of pyridinic/graphitic N.[62,63] However, unlike the aforementioned studies, we find that the catalytic selectivity and activity of bagasse-derived N-doped carbon catalysts are not linearly correlated with the total N, pyridinic N, and graphitic N content. The five best electrocatalysts prepared in this study are selected and compared at the highest j_{CO} (−0.90 V vs. RHE for ANBC6 ($KHCO_3$), −0.91 V vs. RHE for ANBC1 ($NaHCO_3$) and ANBC5 (KOH), −1.00 V vs. RHE for ANBC2 (K_2CO_3), and −1.04 V vs. RHE for ANBC4(NaOH), respectively). The relationship between the total pyridinic and graphitic N content and the FE_{CO} and j_{CO} for these materials is shown in Figure 5. This shows that neither the total N content nor the pyridinic/graphitic N content is positively correlated to the selectivity and activity of the N-doped carbon catalyst. Therefore, overemphasizing the contribution of N-doping is not helpful to understand the structure-activity relationship. Similarly, several studies have reported that lower N-doping levels can lead to a better catalytic performance for the CO_2RR.[77,82] The improvement of CO_2RR performances were attributed to the increased concentration of defects, which were generated by removing N atoms from the N-doped carbon. However, these N atoms generally could not be entirely removed. Therefore, it is difficult to identify whether the N-containing sites or the defect sites are the dominant active sites for the CO_2RR. Although the relationship analysis with limited samples is not perfect, this observation provides direct evidence that the catalytic performance of N-doped carbon materials for CO_2RR is determined by a synergistic effect of different factors and is not solely determined by N-doping content or the configuration of N-dopant. This conclusion is similar to the results of Yao et al.,[60] who reported an N-doped carbon derived from Typha that maintains a large surface area and pore volume but lower N-doping content that outperformed a sample with a higher N-doping level. Although this dataset does not help to understand which nitrogen configuration acts as the real active sites, it highlights the trade-off between N loading content and the microstructures of the carbon catalysts.

A larger specific surface area of the catalysts exposes more active sites and thus enhances the catalytic performance for CO_2RR. When the specific surface area of the catalyst is small, other advantageous factors are suppressed, resulting in poor catalytic performance, such as is the case for NBC, ANBC2 (K_2CO_3) and ANBC3 ($Mg_5(OH)_2(CO_3)_4$). However, this does not mean that the larger specific surface always leads to better catalytic performances.[40] As shown in Figure S14a, there is no direct correlation between the performance of the catalysts and the specific surface area. Similarly, the electrochemical performance does not show a positive correlation with the electrochemically active surface area (Figure S14b). Not all electrochemically active sites are catalytically active toward the CO_2RR and not all of the CO_2 can be effectively transported to the

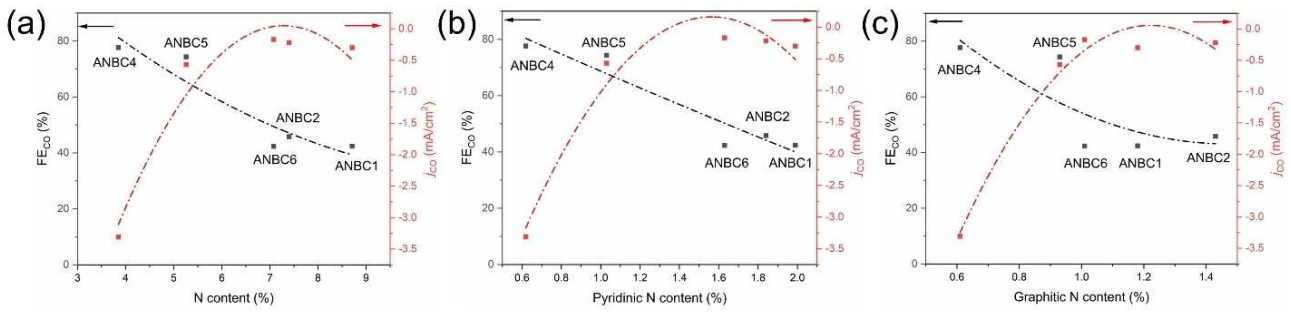

Figure 5. The relationship between electrochemical performance and (a) total N content; (b) pyridinic N content; (c) graphitic N content.

active sites of the N-doped carbon catalyst. Many studies have indicated that the porous structure plays an important role in the mass transfer of reactants and products, and electrolyte diffusion processes.[33,60] Several studies have pointed out that a hierarchically porous structure helps to improve the performance of N-doped carbon catalysts for CO_2RR in the aqueous phase. Macropores and mesopores act as a reservoir to minimize the diffusion distance of reactants and electrolytes, which facilitates the mass transfer process, while micropores provide a large specific surface area and expose more active sites, further enhancing the CO_2RR performance of N-doped carbon materials.[44] Among the porous structures, the availability of mesopores is considered a key factor determining the overall performance. Ma et al. verified that catalysts with higher mesoporous content exhibit better performance for CO_2RR by electrochemical impedance spectroscopy (EIS) tests and suggested that the mesoporous structure allows more active sites to be exposed to the electrolyte and accelerates the diffusion of the electrolyte to those active sites.[83] Hursán et al.[84] indicated that the selectivity, activity, and stability of the CO_2RR on N-doped carbon catalysts are highly dependent on the porosity. The results obtained in this study are consistent with these reports. ANBC4 (NaOH) shows the best electrocatalytic performance with a 3.85% N-doping, 1277.94 $m^2 g^{-1}$ specific surface area and 17.3% mesopores. Although ANBC5 (KOH) and ANBC6 ($KHCO_3$) show a larger specific surface area and higher N-doping level than ANBC4 (NaOH), their electrocatalytic performances are worse. This can be attributed to the lower mesopore ratios (12.5% and 11.3%, respectively) in ANBC5 (KOH) and ANBC6 ($KHCO_3$) that hinder the mass transfer of reactants to the active sites.

The degree of graphitization is also considered to be one of the important factors affecting catalytic performance, as a higher degree of graphitization can be beneficial to improve electron transfer during CO_2RR.[39] N-doping, activation processes, and pyrolysis temperature all have significant effects on the degree of graphitization. Anthony et al.[20] point out that a delicate balance between the N-doping level and the degree of graphitization is essential, with sufficient N sites helping to improve catalytic activity, but an excessive number of N sites reduces the degree of graphitization, negatively affecting the conductivity and charge transfer. A strong activator induces lots of defects into the carbon material, which improves the specific surface area but reduces the degree of graphitization.[34] In addition, high pyrolysis temperatures promote the structural alignment of carbon materials but will remove the heteroatoms, generating a more disordered carbon lattice.[34] In this study, most of the catalysts showed similar degrees of graphitization due to the application of the same pyrolysis temperature and N-doping strategy. Notably, ANBC3 ($Mg_5(OH)_2(CO_3)_4$) exhibited the lowest degree of graphitization and specific surface area and therefore, despite its high mesopores ratio, displayed the worst catalytic performance.

Conclusion

In conclusion, we have prepared a series of N-doped carbon catalysts derived from sugarcane bagasse, carbonized, and activated with different activators, to investigate the specific effect that these activators have on the overall CO_2RR performance of the resulting carbon catalysts. The textural properties of the carbon catalysts are highly dependent on the type of activator used, which further affects the electrochemical performance. The obtained results show that the CO_2RR performance of the carbon-based catalysts did not solely depend on the N-doping level or the configuration of N-dopants, but the synergistic effects of the N-doping, the specific surface area, the porosity, and the degree of graphitization jointly determines the catalytic performance. The ratio of mesoporosity is demonstrated as an important parameter that can enhance the mass transfer and improve the accessibility of the reactant to the active sites. The degree of graphitization affects the conductivity of carbon catalysts, with a higher degree of graphitization leading to higher current densities for CO_2RR. In this study, different activators endow the carbon catalysts with various physicochemical properties, thus exhibiting significant differences in electrochemical performance for CO_2RR. Among them, sodium hydroxide has been demonstrated as the most effective activator, endowing the carbon catalyst with a proper N-doping content, large surface area, abundant pores with high mesoporosity, and relatively higher degree of graphitization, enabling it to reach a high performance for CO_2RR with 80% faradaic efficiency towards CO at −0.93 V vs. RHE. This work presents a comprehensive analysis of the function of different activators on N-doped carbon catalysts for CO_2RR, which can provide guidance for the design and synthesis of high-performance N-doped carbon catalysts.

Experimental Section

Materials and chemicals

Sugarcane bagasse, which mainly consists of lignocellulose, was collected from a sugarcane processing factory (India, Maharashtra). The abundant natural vascular fiber bundles in bagasse make it a good precursor to prepare the porous carbon materials. The material was milled and sieved to obtain a particle size class smaller than 425 μm and dried overnight at 105 °C in an oven (BINDER, Model E28). In this work, urea was used as an additive N source to provide additional nitrogen doping.

The activators, such as potassium carbonate (K_2CO_3, 99%), potassium bicarbonate ($KHCO_3$, 99.7%), potassium hydroxide (KOH, 98%), sodium bicarbonate ($NaHCO_3$, 99.7%), sodium hydroxide (NaOH, 98%), magnesium carbonate hydroxide pentahydrate ($Mg_5(OH)_2(CO_3)_4 \cdot 5H_2O$, Bioxtra), and the auxiliary chemicals, such as hydrochloric acid (HCl, 37%), urea (CN_2H_4O, 99%), isopropanol (C_3H_8O, 99.9%) and Nafion perfluorinated resin solution (5 wt.% in lower aliphatic alcohols and 15–20% water) were all purchased from Sigma-Aldrich. Glassy carbon plates polished to a mirror-like finish were purchased from HTW Hochtemperatur-Werkstoffe GmbH (Germany) and used as working electrodes. All chemicals were used as received without further purification. Electrolyte

solutions and 1 M HCl solutions were prepared from ultrapure water (Milli-Q IQ 7000, 18.2 MΩ).

Catalyst preparation

The activated N-doped porous carbon catalysts were prepared using a one-step pyrolysis method. Bagasse (5 g), urea (10 g), and one of the earlier mentioned activators (15 g) were fully mixed with a weight ratio of 1:2:3 and subsequently loaded into a crucible for pyrolysis. The mixtures were carbonized in a muffle furnace (Nabertherm, Model: L9/12/B180, Germany) under a nitrogen atmosphere (N_2, Linde, 99.99%) with a flow rate of 100 mL min^{-1} and a heating rate of 10 °C min^{-1} from ambient temperature to 800 °C, holding the temperature at 800 °C for 1 h. Subsequently, the pyrolyzed carbon materials were washed with a 1 M HCl solution to remove any impurities and washed with ultrapure water until the solution reached a neutral pH. Finally, the activated N-doped carbon catalysts were dried at 105 °C for 12 h in an oven. The obtained biomass-derived carbon catalysts were marked as ANBC1 ($NaHCO_3$), ANBC2 (K_2CO_3), ANBC3 ($Mg_5(OH)_2(CO_3)_4$), ANBC4 (NaOH), ANBC5 (KOH) and ANBC6 ($KHCO_3$), respectively.

For comparison, the original biomass-derived carbon (without urea and activator) and pure N-doped carbon (mixed with urea but without any activator) were prepared using the same procedure, and named BC and NBC, respectively.

Catalyst characterization

The morphology and microstructures of all carbon catalysts were visualized with a JEOL JSM-6500F scanning electron microscope (SEM), operating at an acceleration voltage of 15 kV, and equipped with an energy-dispersive X-ray spectroscopy (EDX) detector (Ultra-dry, ThermoScientific, USA), and a JEOL JEM1400 transmission electron microscope (TEM), operating at a voltage of 120 kV. The pore characteristics of all samples were measured by isothermal N_2 adsorption-desorption at 77 K using a Micromeritics TriStar II 3020 instrument. The samples were outgassed at 300 °C for 15 h before each adsorption test. The specific surface area (S_{BET}) was calculated according to the Brunauer–Emmett–Teller (BET) method and the estimation of pore size distribution plots were generated by applying Density Functional Theory (DFT) modelling. The surface area (S_{micro}) and volume (V_{micro}) of micropores were determined by the t-plot method. The total pore volume (V_{total}) was calculated by single-point adsorption total pore volume analysis. The average pore diameter (D_{avg}) was obtained as 4 V/S_{BET}.

X-ray powder diffraction (XRD) measurements were carried out using a Bruker AXS D2 Phaser. The diffractometer was operated in Bragg-Brentano diffraction mode, with $Cu_{K\alpha}$ radiation at 30 kV and 10 mA. The scanning 2θ angle range was between 10.0° and 90.0° using a step length of 0.020°. Raman spectra were recorded from 1000 to 2000 cm^{-1} on a Horiba Scientific LabRAM HR Evolution Raman Spectroscopy system with an excitation wavelength of 514 nm.

The surface chemical compositions of all carbon catalysts were investigated by X-ray photoelectron spectroscopy (XPS) using a Thermo Scientific Kα system with $Al_{K\alpha}$ radiation (1486.7 eV). Survey scans were performed with a spot size of 200 μm, pass energy of 55 eV, and energy step of 0.1 eV. All binding energies for XPS spectra were calibrated according to the C1s peak at 284.8 eV in CasaXPS.

Electrochemical measurements

The electrochemical performances of different catalysts were evaluated in a gas-tight two-compartment flow cell, where the anode and cathode compartment were separated by a Selemion AMV membrane (AGC group, Japan).[85] Each compartment contained 1.8 mL of 0.1 M $KHCO_3$ electrolyte. A platinum foil (MaTeck GmbH, 99.9%) was used as a counter electrode, while a leak-free Ag/AgCl electrode (Innovative Instruments, Inc.) was used as a reference electrode. The cathode chamber of the cell was purged using CO_2 or Ar, depending on the experiment, with a flow rate of 8 mL min^{-1} for at least 15 min before the electrochemical test.

The working electrode was prepared by drop casting a catalyst ink on a glassy carbon substrate. The catalyst ink was prepared by dispersing 4 mg of catalyst powder in a solvent mixture containing 800 μL deionized water, 150 μL isopropanol, and 50 μL of 5% Nafion solution with sonication for 1 h to obtain a homogeneous ink. Afterwards, 200 μL of the ink was drop-casted on the center of the 25 mm × 25 mm glassy carbon plate and dried at room temperature. The geometric surface area of the working electrode exposed to the electrolyte was equal to 1 cm^2.

The electrochemical measurements were carried out using a Biologic SP-200 potentiostat (Biologic, France), equipped with the software EC-lab (Biologic, France). All applied potentials were converted to the reversible hydrogen electrode (RHE) scale according to Equation (1):

$$E\ (\text{V vs. RHE}) = E\ (\text{V vs. Ag/AgCl}) + 0.197 + 0.059 \times \text{pH} \quad (1)$$

The cell resistance (Ru) was measured by potentiostatic electrochemical impendence spectroscopy (PEIS). 85% of Ru was used to conduct the Ohmic Drop Correction automatically with EC-Lab during CO_2RR, while the remaining 15% was corrected manually afterwards. Linear sweep voltammograms (LSV) were recorded in Ar-saturated (pH 8.3) and CO_2-saturated (pH 6.8) 0.1 M $KHCO_3$ electrolytes at a scan rate of 5 mV s^{-1}. The electrochemically active surface area (ECSA) of the electrode was determined by measuring the double layer capacitance (C_{dl}), which is derived from cyclic voltammetry measurements with a scan rate at 5, 10, 25 and 50 mV s^{-1} in the potential window of 0.45 to 0.55 V vs. RHE. The C_{dl} was estimated by plotting the Δj (j_a-j_c)/2 at 0.50 V vs. RHE against the scan rates, where the slope of the plot gives the C_{dl}.

Chronoamperometry was applied to measure the electrocatalytic performance of different samples over the course of one hour. CO_2 was purged into the catholyte with a flow rate of 8 mL min^{-1} through a mass flow controller. A mass flow meter downstream of the electrochemical cell was inserted to ensure the absence of leakages during the test. The gas-phase products were sampled automatically every 2 min by an online gas chromatograph (Compact GC 4.0, equipped with Rt-QBond columns). A flame ionization detector (FID) was used to measure the hydrocarbon compounds and two thermal conductivity detectors (TCD) were used to measure CO and H_2, respectively. A standard calibration curve, made from gas mixture cylinders with known concentrations (Linde gas Benelux B.V.), was used to calculate the concentration of product gasses in the gas stream. The liquid-phase products were measured by injecting an aliquot of the electrolyte, taken at the end of the measurement, on a high-performance liquid chromatograph (HPLC, Agilent 1260 Infinity). Sample vials were placed in an autosampler and 10 μL was injected onto two Aminex HPX 87-H columns (Biorad) placed in series. During analysis the column oven temperature was maintained constant at 60 °C, with a steady flow of rate of 0.600 mL min^{-1} of an aqueous 1 mM H_2SO_4 eluent.

Acknowledgements

S.F. and M.L acknowledge a PhD scholarship awarded by the China Scholarship Council (CSC). S.A would like to acknowledge funding from TOeLS, an activity co-financed by Shell and a PPP-allowance from Top Consortia for Knowledge and Innovation (TKI's) of the Ministry of Economic Affairs and Climate in the context of the TU Delft e-Refinery program. The authors thank Michel van den Brink for the help in performing the experiments, Willy Rook for the N_2 adsorption/desorption tests and Kees Kwakernaak for the help in SEM morphology characterization.

Conflict of Interest

The authors declare no conflict of interest.

Data Availability Statement

The data that support the findings of this study are available from the corresponding author upon reasonable request.

Keywords: biomass · carbon activation · CO_2 valorization · doping · electrocatalysis

[1] R. Kortlever, J. Shen, K. J. P. Schouten, F. Calle-Vallejo, M. T. M. Koper, *J. Phys. Chem. Lett.* **2015**, *6*, 4073–4082.
[2] C.-T. Dinh, T. Burdyny, M. G. Kibria, A. Seifitokaldani, C. M. Gabardo, F. P. G. De Arquer, A. Kiani, J. P. Edwards, P. De Luna, O. S. Bushuyev, *Science* **2018**, *360*, 783–787.
[3] Y. Y. Birdja, E. Pérez-Gallent, M. C. Figueiredo, A. J. Göttle, F. Calle-Vallejo, M. T. M. Koper, *Nat. Energy* **2019**, *4*, 732–745.
[4] E. V Kondratenko, G. Mul, J. Baltrusaitis, G. O. Larrazábal, J. Pérez-Ramírez, *Energy Environ. Sci.* **2013**, *6*, 3112–3135.
[5] M. Moura de Salles Pupo, R. Kortlever, *ChemPhysChem* **2019**, *20*, 2926–2935.
[6] T. Ma, Q. Fan, H. Tao, Z. Han, M. Jia, Y. Gao, W. Ma, Z. Sun, *Nanotechnology* **2017**, *28*, 472001.
[7] Q. Lu, F. Jiao, *Nano Energy* **2016**, *29*, 439–456.
[8] W. Zhang, Y. Hu, L. Ma, G. Zhu, Y. Wang, X. Xue, R. Chen, S. Yang, Z. Jin, *Adv. Sci.* **2018**, *5*, 1700275.
[9] E. L. Clark, S. Ringe, M. Tang, A. Walton, C. Hahn, T. F. Jaramillo, K. Chan, A. T. Bell, *ACS Catal.* **2019**, *9*, 4006–4014.
[10] Y. Fang, J. C. Flake, *J. Am. Chem. Soc.* **2017**, *139*, 3399–3405.
[11] W. Zhu, S. Kattel, F. Jiao, J. G. Chen, *Adv. Energy Mater.* **2019**, *9*, 1802840.
[12] M. Z. Ertem, S. J. Konezny, C. M. Araujo, V. S. Batista, *J. Phys. Chem. Lett.* **2013**, *4*, 745–748.
[13] T. Zhang, X. Li, Y. Qiu, P. Su, W. Xu, H. Zhong, H. Zhang, *J. Catal.* **2018**, *357*, 154–162.
[14] C. Cui, J. Han, X. Zhu, X. Liu, H. Wang, D. Mei, Q. Ge, *J. Catal.* **2016**, *343*, 257–265.
[15] K. Jiang, Y. Huang, G. Zeng, F. M. Toma, W. A. Goddard III, A. T. Bell, *ACS Energy Lett.* **2020**, *5*, 1206–1214.
[16] T.-C. Chou, C.-C. Chang, H.-L. Yu, W.-Y. Yu, C.-L. Dong, J.-J. Velasco-Vélez, C.-H. Chuang, L.-C. Chen, J.-F. Lee, J.-M. Chen, *J. Am. Chem. Soc.* **2020**, *142*, 2857–2867.
[17] K. Van Daele, B. De Mot, M. Pupo, N. Daems, D. Pant, R. Kortlever, T. Breugelmans, *ACS Energy Lett.* **2021**, *6*, 4317–4327.
[18] C. Hu, L. Dai, *Adv. Mater.* **2019**, *31*, 1804672.
[19] C. Hu, J. Qu, Y. Xiao, S. Zhao, H. Chen, L. Dai, *ACS Cent. Sci.* **2019**, *5*, 389–408.
[20] A. Vasileff, Y. Zheng, S. Z. Qiao, *Adv. Energy Mater.* **2017**, *7*, 1700759.
[21] X. Duan, J. Xu, Z. Wei, J. Ma, S. Guo, S. Wang, H. Liu, S. Dou, *Adv. Mater.* **2017**, *29*, 1701784.
[22] C. Ma, P. Hou, X. Wang, Z. Wang, W. Li, P. Kang, *Appl. Catal. B* **2019**, *250*, 347–354.
[23] H. R. M. Jhong, C. E. Tornow, B. Smid, A. A. Gewirth, S. M. Lyth, P. J. A. Kenis, *ChemSusChem* **2017**, *10*, 1094–1099.
[24] X. Cui, Z. Pan, L. Zhang, H. Peng, G. Zheng, *Adv. Energy Mater.* **2017**, *7*, 1701456.
[25] X. Sun, X. Kang, Q. Zhu, J. Ma, G. Yang, Z. Liu, B. Han, *Chem. Sci.* **2016**, *7*, 2883–2887.
[26] H. Wang, Y. Chen, X. Hou, C. Ma, T. Tan, *Green Chem.* **2016**, *18*, 3250–3256.
[27] H. Wang, J. Jia, P. Song, Q. Wang, D. Li, S. Min, C. Qian, L. Wang, Y. F. Li, C. Ma, T. Wu, J. Yuan, M. Antonietti, G. A. Ozin, *Angew. Chem. Int. Ed.* **2017**, *56*, 7847–7852; *Angew. Chem.* **2017**, *129*, 7955–7960.
[28] Y. Song, W. Chen, C. Zhao, S. Li, W. Wei, Y. Sun, *Angew. Chem. Int. Ed.* **2017**, *56*, 10840–10844; *Angew. Chem.* **2017**, *129*, 10980–10984.
[29] W.-J. Liu, H. Jiang, H.-Q. Yu, *Energy Environ. Sci.* **2019**, *12*, 1751–1779.
[30] Z. Zhang, S. Yang, H. Li, Y. Zan, X. Li, Y. Zhu, M. Dou, F. Wang, *Adv. Mater.* **2019**, *31*, 1805718.
[31] F. Yu, S. Li, W. Chen, T. Wu, C. Peng, *Energy Environ. Mater.* **2019**, *2*, 55–67.
[32] X. Peng, L. Zhang, Z. Chen, L. Zhong, D. Zhao, X. Chi, X. Zhao, L. Li, X. Lu, K. Leng, C. Liu, W. Liu, W. Tang, K. P. Loh, *Adv. Mater.* **2019**, *31*, 1900341.
[33] J. Niu, R. Shao, M. Liu, Y. Zan, M. Dou, J. Liu, Z. Zhang, Y. Huang, F. Wang, *Adv. Funct. Mater.* **2019**, *29*, 1905095.
[34] Q. Niu, K. Gao, Q. Tang, L. Wang, L. Han, H. Fang, Y. Zhang, S. Wang, L. Wang, *Carbon* **2017**, *123*, 290–298.
[35] W. J. Liu, H. Jiang, H. Q. Yu, *Energy Environ. Sci.* **2019**, *12*, 1751–1779.
[36] X. Li, B. Y. Guan, S. Gao, X. W. Lou, *Energy Environ. Sci.* **2019**, *12*, 648–655.
[37] M. Borghei, J. Lehtonen, L. Liu, O. J. Rojas, *Adv. Mater.* **2018**, *30*, 1703691.
[38] F. Li, M. Xue, G. P. Knowles, L. Chen, D. R. MacFarlane, J. Zhang, *Electrochim. Acta.* **2017**, *245*, 561–568.
[39] X. Hao, X. An, A. M. Patil, P. Wang, X. Ma, X. Du, X. Hao, A. Abudula, G. Guan, *ACS Appl. Mater. Interfaces.* **2021**, *13*, 3738–3747.
[40] W. Liu, J. Qi, P. Bai, W. Zhang, L. Xu, *Appl. Catal. B* **2020**, *272*, 118974.
[41] M. Scimeca, S. Bischetti, H. K. Lamsira, R. Bonfiglio, E. Bonanno, *Eur. J. Histochem.* **2018**, *62*, 2841.
[42] M. Thommes, K. Kaneko, A. V Neimark, J. P. Olivier, F. Rodriguez-Reinoso, J. Rouquerol, K. S. W. Sing, *Pure Appl. Chem.* **2015**, *87*, 1051–1069.
[43] Y. Liu, G. Dai, L. Zhu, S. Wang, *ChemElectroChem* **2019**, *6*, 602.
[44] L. Hou, Z. Hu, X. Wang, L. Qiang, Y. Zhou, L. Lv, S. Li, *J. Colloid Interface Sci.* **2019**, *540*, 88–96.
[45] I. Katsounaros, S. Cherevko, A. R. Zeradjanin, K. J. J. Mayrhofer, *Angew. Chem. Int. Ed.* **2014**, *53*, 102–121; *Angew. Chem.* **2014**, *126*, 104–124.
[46] H. Feng, H. Hu, H. Dong, Y. Xiao, Y. Cai, B. Lei, Y. Liu, M. Zheng, *J. Power Sources* **2016**, *302*, 164–173.
[47] H. Li, N. Xiao, M. Hao, X. Song, Y. Wang, Y. Ji, C. Liu, C. Li, Z. Guo, F. Zhang, J. Qiu, *Chem. Eng. J.* **2018**, *351*, 613–621.
[48] P. P. Sharma, J. Wu, R. M. Yadav, M. Liu, C. J. Wright, C. S. Tiwary, B. I. Yakobson, J. Lou, P. M. Ajayan, X. D. Zhou, *Angew. Chem. Int. Ed.* **2015**, *54*, 13701–13705; *Angew. Chem.* **2015**, *127*, 13905–13909.
[49] K. Zou, Y. Deng, J. Chen, Y. Qian, Y. Yang, Y. Li, G. Chen, *J. Power Sources* **2018**, *378*, 579–588.
[50] C. Zhao, Q. Wang, Y. Lu, B. Li, L. Chen, Y.-S. Hu, *Sci. Bull.* **2018**, *63*, 1125–1129.
[51] Y. Li, B. Xing, X. Wang, K. Wang, L. Zhu, S. Wang, *Energy Fuels* **2019**, *33*, 12459–12468.
[52] N. Brun, S. R. S. Prabaharan, C. Surcin, M. Morcrette, H. Deleuze, M. Birot, O. Babot, M.-F. Achard, R. Backov, *J. Phys. Chem. C* **2012**, *116*, 1408–1421.
[53] J. Deng, T. Xiong, F. Xu, M. Li, C. Han, Y. Gong, H. Wang, Y. Wang, *Green Chem.* **2015**, *17*, 4053–4060.
[54] K. Li, W. Chen, H. Yang, Y. Chen, S. Xia, M. Xia, X. Tu, H. Chen, *Bioresour. Technol.* **2019**, *280*, 260–268.
[55] Q. Wang, J. Yan, Y. Wang, T. Wei, M. Zhang, X. Jing, Z. Fan, *Carbon* **2014**, *67*, 119–127.
[56] X. Kang, H. Zhu, C. Wang, K. Sun, J. Yin, *J. Colloid Interface Sci.* **2018**, *509*, 369–383.
[57] L. Wang, W. Yan, C. He, H. Wen, Z. Cai, Z. Wang, Z. Chen, W. Liu, *Appl. Surf. Sci.* **2018**, *433*, 222–231.
[58] J. Liu, Y. Deng, X. Li, L. Wang, *ACS Sustainable Chem. Eng.* **2016**, *4*, 177–187.
[59] W. Yu, F. Lian, G. Cui, Z. Liu, *Chemosphere* **2018**, *193*, 8–16.

[60] P. Yao, Y. Qiu, T. Zhang, P. Su, X. Li, H. Zhang, *ACS Sustainable Chem. Eng.* **2019**, *7*, 5249–5255.
[61] R. Paul, L. Zhu, H. Chen, J. Qu, L. Dai, *Adv. Mater.* **2019**, *31*, 1806403.
[62] M. Kuang, A. Guan, Z. Gu, P. Han, L. Qian, G. Zheng, *Nano Res.* **2019**, *12*, 2324–2329.
[63] Z. Zhang, L. Yu, Y. Tu, R. Chen, L. Wu, J. Zhu, D. Deng, *Cell Rep.* **2020**, *1*, 100145.
[64] B. Duan, X. Gao, X. Yao, Y. Fang, L. Huang, J. Zhou, L. Zhang, *Nano Energy* **2016**, *27*, 482–491.
[65] J. Przepiórski, J. Karolczyk, K. Takeda, T. Tsumura, M. Toyoda, A. W. Morawski, *Ind. Eng. Chem. Res.* **2009**, *48*, 7110–7116.
[66] G. Dobele, T. Dizhbite, M. V Gil, A. Volperts, T. A. Centeno, *Biomass Bioenergy* **2012**, *46*, 145–154.
[67] O. Pezoti, A. L. Cazetta, K. C. Bedin, L. S. Souza, A. C. Martins, T. L. Silva, O. O. S. Júnior, J. V Visentainer, V. C. Almeida, *Chem. Eng. J.* **2016**, *288*, 778–788.
[68] T. Ouyang, T. Zhang, H. Wang, F. Yang, J. Yan, K. Zhu, K. Ye, G. Wang, L. Zhou, K. Cheng, *Chem. Eng. J.* **2018**, *352*, 459–468.
[69] S. Yu, N. Sun, L. Hu, L. Wang, Q. Zhu, Y. Guan, B. Xu, *J. Power Sources* **2018**, *405*, 132–141.
[70] T. Wu, G. Wang, Q. Dong, F. Zhan, X. Zhang, S. Li, H. Qiao, J. Qiu, *Environ. Sci. Technol.* **2017**, *51*, 9244–9251.
[71] M. Sevilla, A. B. Fuertes, *ChemSusChem* **2016**, *9*, 1880–1888.
[72] J. Deng, T. Xiong, H. Wang, A. Zheng, Y. Wang, *ACS Sustainable Chem. Eng.* **2016**, *4*, 3750–3756.
[73] H. Arslanoğlu, *J. Hazard. Mater.* **2019**, *374*, 238–247.
[74] W. Li, B. Herkt, M. Seredych, T. J. Bandosz, *Appl. Catal. B* **2017**, *207*, 195–206.
[75] E. Taer, A. Agustino, R. Farma, R. Taslim, M. Paiszal, A. Ira, S. D. Yardi, Y. P. Sari, H. Yusra, S. Nurjanah, *J. Phys. Conf. Ser.* **2018**, *1116*, 32040.
[76] D. Voiry, M. Chhowalla, Y. Gogotsi, N. A. Kotov, Y. Li, R. M. Penner, R. E. Schaak, P. S. Weiss, *ACS Nano* **2018**, *12*, 9635–9638.
[77] R. Daiyan, X. Tan, R. Chen, W. H. Saputera, H. A. Tahini, E. Lovell, Y. H. Ng, S. C. Smith, L. Dai, X. Lu, R. Amal, *ACS Energy Lett.* **2018**, *3*, 2292–2298.
[78] Y. Dong, Q. Zhang, Z. Tian, B. Li, W. Yan, S. Wang, K. Jiang, J. Su, C. W. Oloman, E. L. Gyenge, R. Ge, Z. Lu, X. Ji, L. Chen, Y. Dong, Q. Zhang, Z. Tian, B. Li, S. Wang, K. Jiang, J. Su, R. Ge, Z. Lu, L. Chen, C. W. Oloman, E. L. Gyenge, W. Yan, X. Ji, *Adv. Mater.* **2020**, *32*, 2001300.
[79] K. A. Adegoke, N. W. Maxakato, *Mater. Today Chem.* **2022**, *24*, 100838.
[80] H. Wang, T. Maiyalagan, X. Wang, *ACS Catal.* **2012**, *2*, 781–794.
[81] H. Wang, J. Jia, P. Song, Q. Wang, D. Li, S. Min, C. Qian, L. Wang, Y. F. Li, C. Ma, *Angew. Chem. Int. Ed.* **2017**, *56*, 7847–7852; *Angew. Chem.* **2017**, *129*, 7955–7960.
[82] W. Wang, L. Shang, G. Chang, C. Yan, R. Shi, Y. Zhao, G. I. N. Waterhouse, D. Yang, T. Zhang, *Adv. Mater.* **2019**, *31*, 1808276.
[83] X. Ma, J. Du, H. Sun, F. Ye, X. Wang, P. Xu, C. Hu, L. Zhang, D. Liu, *Appl. Catal. B* **2021**, *298*, 120543.
[84] D. Hursán, A. A. Samu, L. Janovák, K. Artyushkova, T. Asset, P. Atanassov, C. Janáky, *Joule* **2019**, *3*, 1719–1733.
[85] P. Lobaccaro, M. R. Singh, E. L. Clark, Y. Kwon, A. T. Bell, J. W. Ager, *Phys. Chem. Chem. Phys.* **2016**, *18*, 26777–26785.

Manuscript received: November 24, 2022
Revised manuscript received: January 30, 2023
Accepted manuscript online: January 31, 2023
Version of record online: March 23, 2023